Acta Pharmaceutica Sinica B 2024;14(7):3251−3265

Chinese Pharmaceutical Association
Institute of Materia Medica, Chinese Academy of Medical Sciences

Acta Pharmaceutica Sinica B

www.elsevier.com/locate/apsb
www.sciencedirect.com

ORIGINAL ARTICLE

Sequential dual-locking strategy using photoactivated Pt(IV)-based metallo-nano prodrug for enhanced chemotherapy and photodynamic efficacy by triggering ferroptosis and macrophage polarization

Jun Li[a], Qiang Zhang[a], Hao Yang[a], Wenli Lu[a], Yulong Fu[b], Yingcai Xiong[a], Xuan Wang[a], Tianming Lu[a], Yanlin Xin[a], Zejuan Xie[a], Weichao Chen[c,*], Guoqiang Wang[b,*], Yuanyuan Guo[a,*], Ruogu Qi[a,*]

[a]*School of Medicine, Nanjing University of Chinese Medicine, Nanjing 210023, China*
[b]*Key Laboratory of Mesoscopic Chemistry of Ministry of Education, Institute of Theoretical and Computational Chemistry, School of Chemistry and Chemical Engineering, Nanjing University, Nanjing 210023, China*
[c]*Laboratory for Manufacturing Low Carbon and Functionalized Textiles, College of Textiles & Clothing, Qingdao University, Qingdao 266071, China*

Received 13 November 2023; received in revised form 11 January 2024; accepted 8 February 2024

KEY WORDS

Dual-locking;
Pt(IV) reduction;
Chemotherapy;
Photodynamic therapy;
Ferroptosis;
Macrophage polarization;
Medicinal inorganic chemistry;

Abstract Selective activation of Pt(IV) prodrugs within tumors has emerged as a promising strategy in tumor treatment. Although progress has been made with photo- and ultrasound-activated Pt(IV) prodrugs, concerns remain over the non-specific activation of photosensitizers (PS) and the potential for phototoxicity and chemical toxicity. In this study, a sequential dual-locked Pt(IV) nano-prodrug that can be activated by both the acidic tumor microenvironment and light was developed. The Pt(IV) prodrug was prepared by conjugating PS-locked Pt(IV) to a polymeric core, which was then chelated with metallo iron to lock its photoactivity and form a metallo-nano prodrug. Under acidic tumor microenvironment conditions, the metallo-nano prodrug undergoes dissociation of iron, triggering a reduction process in oxaliplatin under light irradiation, resulting in the activation of both chemotherapy and photodynamic therapy

*Corresponding authors.
E-mail addresses: chenwc@qdu.edu.cn (Weichao Chen), wangguoqiang710@nju.edu.cn (Guoqiang Wang), guoyy@njucm.edu.cn (Yuanyuan Guo), rqi@njucm.edu.cn (Ruogu Qi).

Peer review under the responsibility of Chinese Pharmaceutical Association and Institute of Materia Medica, Chinese Academy of Medical Sciences.

https://doi.org/10.1016/j.apsb.2024.02.024

Metals in medicine

(PDT). Additionally, the prodrug could induce metallo-triggered ferroptosis and polarization of tumor-associated macrophages (TAM), thereby enhancing tumor inhibition. The dual-lock strategy employed in a nanoparticle delivery system represents an expansion in the application of platinum-based anticancer drugs, making it a promising new direction in cancer treatment.

1. Introduction

Platinum(II)-based drugs are widely used for treating cancer, but their application is limited by toxicity and resistance[1,2]. One strategy to overcome the limitations of platinum(II) compounds like oxaliplatin is to convert them into platinum(IV) prodrugs, which are generally less toxic and have potential advantages in cancer treatment[3-6]. Thus, the key challenge with Pt(IV) prodrugs is their conversion into the active platinum(II) form within cancer cells. This conversion is essential for the drug to exert its anticancer effects. The intracellular reduction of Pt(IV) prodrugs into the active platinum(II) agent relies on the presence of reducing agents like glutathione (GSH), metallothionein, or ascorbic acid within cancer cells[7,8]. However, the presence and concentration of these reducing agents can vary among different tumor sites, leading to variability in the efficiency of the Pt(IV) reduction process[9,10].

To overcome this limit, structural modifications of platinum(II) agents are made to the functional platinum(IV) prodrug, with the specific aim of rapid reduction of Pt(IV)[11-13]. The most promising approach revolves around harnessing the electron transfer properties of sensitizer ligands containing Pt(IV) prodrugs that respond to either light or intense ultrasound, which allows activation upon exposure to either light or high-intensity ultrasound (US)[14-17]. The photoelectrons of the ligands were received by the Pt(IV) prodrugs and then reduced to Pt(II) complexes[18]. Meanwhile, the combination of light or ultrasound for photodynamic therapy (PDT) or sonodynamic therapy (SDT) has emerged as a promising cancer treatment method[17,19-23]. While the controlled reduction of the Pt(IV) prodrugs and PDT or SDT controlled by exogenous activators with the advantage of high spatial and temporal, there are still hidden drawbacks: 1) non-specific accumulation and activation of photosensitizer or sonosensitizers united Pt(IV) owing to shortage of targeting-tumor and low light-stimulation were still existed phototoxicity or chemotherapy toxicity in normal tissues[24]. 2) in-activation of photosensitizer or sonosensitizers together with Pt(IV) prodrug induced by endogenous GSH in complex tumor microenvironment, which weakens the effect of PDT or SDT or reduction of the Pt(IV) prodrugs[25]. For these reasons, Pt(IV) prodrug that can specifically accumulate in the target area and be controllably activated conveniently is highly demanded.

Ferroptosis is a type of programmed cell death induced by the iron-dependent accumulation of lipid peroxides, which improves anticancer efficacy of PDT and chemotherapy through multiple pathways by increasing oxygen and reactive oxygen species (ROS) or reducing GSH levels[26,27]. Moreover, the potential of ferroptosis synergized with PDT to augment macrophage polarization holds particular significance within the context of cancer immunotherapy[28]. Harnessing this interplay presents a compelling avenue for cancer therapeutic strategies by improving the PDT and chemotherapy.

Herein, a dual-lock strategy is proposed to activate Pt(IV) prodrug sequentially and precisely deliver platinum drugs into tumors, enabling safe and effective cancer therapy (Scheme 1A and B). The strategy involves administering a cationic polymeric core comprised of polyaspartamide (P1) and methoxy polyethylene glycol (mPEG) with a photosensitizer (Ce6) tandem Pt(IV) conjugation prodrug (NP). Subsequently, Fe^{3+} ions coordinate with the carboxyl groups of Ce6 in NP, and the phenolic hydroxyl group of gallic acid (GA) coordinates with Fe-based NP-Fe to form mixed coordination centers of Fe^{3+} (NP-G-Fe). Additionally, PEG-modified chondroitin sulfate (PEG-CS) was coated to NP-G-Fe to enhance tumor targeting and biocompatibility, resulting in the metallo-nano prodrug (NPS-G-Fe). In this strategy, Fe serves to quench the fluorescence and inactivate the photoactivity of Ce6 molecules, acting as the first lock (metallo lock), while Ce6 acts to prevent premature reduction of Pt(IV) without light irradiation, serving as the second lock (light lock). The dual-locked strategy is designed to prevent both the photobleaching of Ce6 and the premature reduction of Ce6−Pt(IV), thus mitigating the risk of unexpected toxicity (Scheme 1A). Upon accumulation in the tumor site, the coordinated GA and Fe^{3+} are dissociated from Ce6−Pt(IV) by the acidic conditions of the tumor microenvironment and intracellular lysosome (first unlock). This step allows for the activation of Ce6−Pt(IV) upon red light irradiation, initiating photodynamic therapy and chemotherapy by generating reactive oxidized species (ROS) and transferring photoelectrons from ligands to reduce Pt(IV) into Pt(II) complexes, respectively (second unlock). Additionally, the released GA expedites the reduction of Fe^{3+} into Fe^{2+} and the depletion of intracellular GSH thereby increasing the treating efficacy by triggering the ferroptosis process and macrophage polarization in cancer cells (Scheme 1B). This approach resulting in increased selectivity and specificity provides a promising strategy for precise cancer therapy.

2. Material and methods

2.1. Materials

Chlorin e6 (Ce6), Iron chloride hexahydrate ($FeCl_3 \cdot 6H_2O$), gallic acid (GA), 1,10-phenanthroline monohydrochloride monohydrate, chondroitin 4-sulfate sodium salt (CS), methoxy polyethylene glycol (mPEG-5000), thiazolyl blue tetrazolium bromide (MTT), L-aspartic acid benzyl ester (Asp(Bzl)), $mPEG_{5k}$-NH_2 and *o*-(benzotriazol-1-yl)-*N*,*N*,*N*′,*N*′-tetramethyluronium tetrafluoroborate (TBTU) were purchased from Macklin, Shanghai, China.

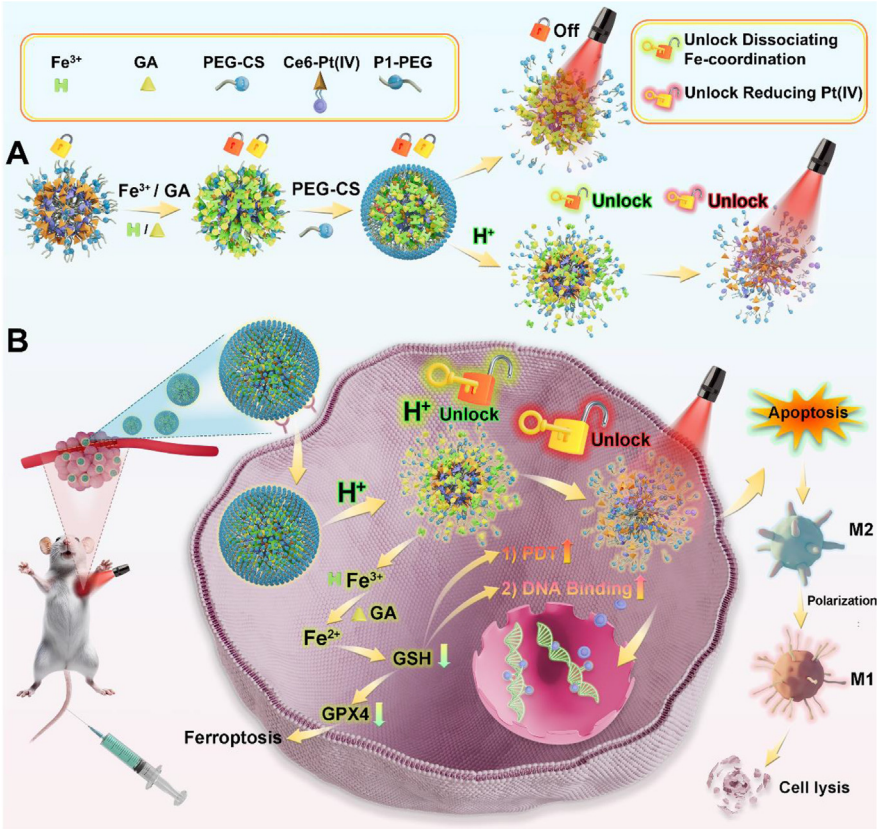

Scheme 1 Schematic illustration of preparation, unlocking process, and biological mechanism of NPS-G-Fe. (A) Preparation and unlocking process of NPS-G-Fe. NP acting second lock was further coordinated with Fe^{3+} coordinated with GA to form a dual lock (NPS-G-Fe). Sequential unlocking NPS-G-Fe was performed by acid condition and red light. (B) NPS-G-Fe was selectively accumulated in the tumor and ingested tumor cells. After being taken up into cells, NPS-G-Fe was dissociated by acid condition to unlock the first lock and subsequently unlock the second lock by red light, initiated PDT, chemotherapy, and ferroptosis to induce apoptosis of tumor cells and cause macrophage polarization.

Oxaliplatin was purchased from Shandong Bayan Pharmaceutical Co., Ltd., Shandong, China. Succinic anhydride, *N*-(3-dimethylaminopropyl)-*N*′-ethylcarbodiimide hydrochloride (EDC), 4-dimethylaminopyridine (DMAP), hydrogen peroxide (H_2O_2), and *N*-hydroxysuccinimide (NHS) were purchased from Aladdin, Shanghai, China. DNA purification Kit, DAPI dihydrochloride, Calcein/PI Live/Dead Viability/Cytotoxicity assay Kit, Active oxygen species (ROS) assay Kit (DCFH-DA), TUNEL apoptosis assay Kit, Glutathione (GSH) assay Kit, and Lipopolysaccharide (LPS) were purchased from Beyotime, Shanghai, China. Interleukin-4 (IL-4) was purchased from Genescript Biotechnology Co., Ltd., Nanjing, China. Creatinine (CR) assay kit, Alanine aminotransferase (ALT) assay Kit, and Total Bilirubin (T-BIL) Kit were purchased from Nanjing Jiancheng Bioengineering Institute, Nanjing, China. Ferrous Iron Colorimetric (Fe^{2+}) assay Kit was purchased from Elabscience Biotechnology Co., Ltd., Wuhan, China. Antibodies for GPX4, FITC-goat anti-mouse IgG, HRP-goat anti-mouse IgG, and TRITC-goat anti-mouse IgG were purchased from AB Clonal, Wuhan, China. Annexin V-FITC/PI apoptosis detection Kit was purchased from Vazyme, Nanjing, China. Antibody for CD206 was purchased from Santa Cruz, TX, USA. Antibody for INOS was purchased from Abcam, Cambridge, UK. Antibody for APC anti-mouse CD206, KIRAVIA Blue 520 anti-mouse F4/80, PE anti-mouse CD86, and Brilliant Violet 421 anti-mouse CD11b were purchased from Biolegend, CA, USA. Primers for *Inos* (F: TTT GCTCATGACATCGACCAGAA; R: CGTTTCGGGATCTGAAT GTGATG) and *Arg1* (F: GTAGACCCTGGGGAACACTAT; R: ATCACCTTGCCAATCCCCAG) were purchased from Tsingke Biotechnology Co., Ltd., Nanjing, China.

2.2. *General measurements*

^1H and ^{13}C NMR spectra were performed by 600 MHz NMR spectrometer (Bruker, MA, USA). The molecular weight for synthesized small molecules was measured by high-resolution mass spectrometry (HR-MS) (Agilent 6546 TOF LC−MS spectrometer, CA, USA). High-performance liquid phase spectroscopy analysis was detected by Thermo Ultimate 3000 High-Performance Liquid Chromatography (HPLC, MA, USA). Coupled Plasma Mass Spectrometer (Agilent Technologies 7700, CA, USA) was used for quantitative analysis of the total platinum and iron contents from different samples, cells, and organs. Ultraviolet absorbance spectrum and fluorescence excitation spectrum were measured by a multifunctional microplate reader (EnVision, PerkinElmer, MA, USA). The size and zeta potential for nanoparticles were detected by Malvern Zetasizer (Nano ZS, Malvern, U.K). The size and morphology of nanoparticles were measured by Transmission Electron Microscopy (TEM, EI-TALOS-F200X, 200 kv, Thermo, MA, USA). Molecular valence

for Pt was analyzed by X-ray Photoelectron Spectroscopy (XPS) (Thermofisher Escalab 250xi, MA, USA). The light activation for NPS both *in vitro* and *in vivo* was performed by 660 nm laser light (MDL-MD-660-1W, Changchun, China). Flow cytometric analysis for cells and animals was performed by multicolor analytical flow cytometry (Beckman, Gallios, CA, USA). MTT and Kit detection (GSH, Fe^{2+}, ALT, CR, T-BIL) analysis were performed using the multifunctional microplate reader (EnVision, PerkinElmer). Fluorescence imaging for cells and tissue slices was visualized by Thunder widefield high-resolution imaging system (Leica, Thunder, Witzler, Germany). *In vivo* imaging of small animals was performed by the small animal *in vivo* imaging system (IVIS Lumina XRMS, PerkinElmer, MA, USA). Gene expression levels for *Inos* and *Arg1* were detected by reverse transcription-polymerase chain reaction (RT-PCR) (Bio-RAD, CA, USA). Protein expression of GPX4 was detected by a Gel imaging system (Bio-RAD).

2.3. Characterization of nano prodrug

The size and zeta potential of NPS-G-Fe were analyzed through Malvern Zetasizer with 660 nm, He−Ne laser, 90 of measurement angle. Size, morphology, and element composition of NPS-G-Fe were detected by TEM or TEM mapping.

2.4. UV−Vis and fluorescence spectrum of nano prodrug

The NPS-G-Fe for UV absorption and fluorescence excitation spectra under different conditions were measured by a multifunctional microplate reader. Briefly, NPS-G-Fe was treated with different acid conditions (pH 6.5, 5.5, and 4.5) or different times of light activation (5, 10, 30 min) (a 660 nm laser, 0.8 W/cm^2) or different acid conditions added light activation to analyze the spectra.

2.5. Analysis content of Fe^{2+} in nano prodrug

The content of Fe^{2+} in NPS-G-Fe under acid conditions (pH 4.5, 5.5, and 6.5) was detected by 1,10-phenanthroline. Simply, the 1,10-phenanthroline was added into the various NPS-G-Fe solutions (pH 4.5, 5.5, and 6.5) and the change of colors of the solution was observed.

2.6. Cell lines and culture conditions

Mice colorectal cancer cells (CT26), mice breast cancer cells (4T1), human colorectal cancer cells (HCT116), and mice monocyte/macrophage cells (raw.264) were cultured with DMEM containing 10% FBS (*v*/*v*) and 1% penicillin and streptomycin (100 μg/mL) at 37 °C and 5% CO_2.

2.7. Cells vitality analysis

Cell vitality analysis was performed using an MTT experiment. CT26, 4T1, and HCT116 cells were seeded in 96 well plates (5×10^3 per well) and cultured for 12 h. Then the cells were treated with various Pt-containing compounds for 4 h. Then, the cells were irradiated with a 660 nm laser (0.8 W/cm^2, 5 min). After 48 h of light activation, the MTT solution (0.5 mg/mL) was added into the wells to incubate 4 h. Then, the absorbance of the plates was measured by a multifunctional microplate reader at 570 nm (peak absorbance) and 650 nm (background absorbance).

2.8. Therapeutic evaluation on CT26 multicellular cancer spheroids (MCSs)

The 3% agarose gel (*w*/*v*) was added to the 24-well plates. CT26 cells were added to the 24-well plates (1×10^3 per well) and cultured for 48 h. Then the CT26 MSCs were treated with various Pt-containing compounds for 6 h. Then, the cells were irradiated with a 660 nm laser (0.8 W/cm^2, 5 min). The changes in CT26 MCSs were observed by optical microscopy on Days 1, 2, 3, 4, 5, 6, and 7.

2.9. Apoptosis detection of CT26 cells using Calcein-AM/PI staining and FLM

The cover slices were placed into the 24-well plates. CT26 cells were seeded in the 24 -well plates and incubated overnight (2×10^4 per well). Then the cells were incubated with various Pt-containing compounds for 4 h and irradiated with a 660 nm laser (0.8 W/cm^2, 5 min). After 24 h of light activation, the cells in the wells were treated with the AM/PI staining solution for 30 min. After that, the staining solution in the well plates was discarded and then the cells were washed with PBS. The fluorescence imaging of the cells was observed by thunder widefield high-resolution imaging system (Calcein-AM, $\lambda_{ex} = 488$ nm; PI, $\lambda_{ex} = 530$ nm).

2.10. Detection of cellular uptake and ROS generation for platinum in CT26 cells

The CT26 cells were seeded into 6-well plates (5×10^5 per well) overnight. Then, CT26 cells were treated with various Pt-containing compounds for 4 h. Then, the culture medium in the well plates was discarded and then the cells in the well plates were washed with PBS. The content of protein for part cells in the wells was detected by Nanodrop (Thermo Scientific, MA, USA). Subsequently, the cells were dissolved by aqua regia until digestion to quantify the content of Pt by ICP-MS.

The cover slices were placed into the 24-well plates. Meanwhile, the CT26 cells were seeded in 24-well plates and cultured overnight (2×10^4 per well). Then, the cells were treated with various Pt-containing compounds for 4 h. After that, the CT26 cells in plates were irradiated with 660 nm laser (0.8 W/cm^2, 5 min). Simultaneously, The DCFH-DA probe was added to the well plates to incubate for 30 min in the incubator. After 30 min, the DCFH-DA staining solution in the wells plates was removed and then the cells were washed with PBS. After that, the cells were fixed with 4% paraformaldehyde for 10 min and then washed by PBS. Subsequently, DAPI was added into the well-plated to stain cell nucleus for 5 min and then cells were washed by PBS. Finally, fluorescence imaging was collected by a Thunder imaging system (DAPI, $\lambda_{ex} = 405$ nm; DCFH-DA, $\lambda_{ex} = 488$ nm; Ce6, $\lambda_{ex} = 530$ nm).

2.11. Analysis of GSH and Fe^{2+} content in CT26 cells

The CT26 cells were seeded in 6 well plates (5×10^5 per well). After 12 h, the CT26 cells in wells were incubated with various Pt-containing compounds for 4 h. After incubation for 4 h, the cells were irradiated with a 660 nm laser (0.8 W/cm^2, 5 min). After

24 h, the culture medium in the well plates was removed and then the cells were washed by PBS. Finally, the intracellular content of GSH and Fe^{2+} was analyzed by a kit of GSH and Fe^{2+}.

2.12. Light-activated platinum and DNA binding

The CT26 cells were seeded in 6 well plates (5×10^5 per well) to culture 12 h. After that, the CT26 cells in wells were treated with various Pt-containing compounds and for incubated 4 h. Then, the cells in well plates were irradiated with a 660 nm laser (0.8 W/cm^2, 5 min). After 12 h of treatment, the culture medium in the well plates was removed and then the cells were washed by PBS. Subsequently, the DNA of the cells was extracted by a DNA extract kit. The content of DNA was analyzed by Nanodrop (Thermo Scientific). Finally, the DNA was dissolved by aqua regia to detect the content of Pt using ICP-MS.

2.13. Detection of protein expression of GPX4 by Western blot

The CT26 cells were seeded in 6-well plates (5×10^5 per well) for 12 h. After that, the CT26 cells were incubated with various Pt-containing compounds to incubate 4 h. After 4 h of incubation, the cells in the well plates were irradiated with 660 nm laser (0.8 W/cm^2, 5 min). After 24 h of light activation, the culture medium in the well plates was removed and the then cells were washed by PBS. Subsequently, the cells were collected and incubated with RIPA lysate buffer for 40 min on ice to obtain protein. After that, the content of the protein was measured by Nanodrop. Then, the protein was isolated by sodium lauryl sulfate-polyacrylamide gel electrophoresis (SDS-PAGE) and migrated to a polyvinylidene fluoride membrane (PVDF). Subsequently, the protein in PVDF membranes was incubated with primary GPX4 antibody at 4 °C for 12 h, and then further incubated with HRP conjugated secondary antibody for 2 h at room temperature. Finally, the signal of fluorescence on the membranes was detected by ECL luminescent solution and visualized by Bio-Rad gel imaging system.

2.14. Macrophage polarization effect

Firstly, the CT26 cells were seeded in 6-well plates (5×10^5 per well) to culture 12 h. Then, CT26 cells were treated with various Pt-containing compounds for 4 h. After that, the cells in the well plates were irradiated with 660 nm laser (0.8 W/cm^2, 5 min) for 24 h. Meanwhile, raw. 264 cells were seeded in 6-well plates (5×10^5 per well) overnight. Then, IL-4 (50 ng/mL) was added to the well plates of macrophages for 24 h to establish the M2 macrophage model. Subsequently, supernatant medium extracted from CT26 cells after treatment with various formulations and light activation or dark was added into the well plates with M0 or M2 macrophages to stimulate 24 h. Then, the cells were collected and the gene expression of *Arg1* and *Inos* was performed by real-time reverse transcription-polymerase chain reactions (RT-PCR).

2.15. Animal welfare and protocols

Male BALB/c mice were purchased from Qing Long Shan Animal Breeding Farm and fed in an SPF environment. All experimental procedures were executed according to the protocols (202302A047) approved by the Nanjing University of Chinese Medicine Animal Care and Use Committee.

2.16. Establishment of CT26 colorectal cancer model

CT26 cells (1×10^6) were resuspended in 100 μL of PBS were injected into the armpit of BALB/c mice. After Day 7, the tumor volumes reached 100 mm^3, which acted as the CT26 colorectal cancer model.

2.17. Biodistribution imaging of CT26 colorectal cancer model

Biodistribution for nano prodrug was evaluated by the CT26 colorectal cancer model when the tumor volume of the mice reached 400 mm^3. The mice were injected with a single dose of FNPS-G-Fe (Pt 3 mg/kg) *via* tail veins. At various times (4, 12, 24, and 48 h), the mice were separately imaged *in vivo* using the small animal *in vivo* imaging system (IVIS Lumina XRMS, PerkinElmer). After 48 h, the mice were sacrificed to collect the heart, liver, spleen, lungs, kidneys, and tumors, which were used for biodistribution imaging. Meanwhile, the content of Pt and Fe within the heart, liver, spleen, lungs, kidneys, and tumors were analyzed by ICP-MS after being digested by aqua regia.

2.18. Anticancer evaluation in CT26 colorectal cancer model

When the tumor volume reached 100 mm^3, the mice were randomly divided into eight groups ($n = 12$). The drugs were injected into the mice once every 3 days *via* tail veins. All groups were: 1) The control group (200 μL of PBS), 2) OXA (oxaliplatin, 3 mg Pt/kg), and 3) various Pt-containing nanoparticles (3 mg Pt/kg). After 4 h of administration, the tumor of the mice was irradiated by 660 nm laser light (0.8 W/cm^2, 5 min). The body weight and tumor volume of the mice were recorded every day and calculated using Eq. (1):

$$\text{Tumor volume} = 1/2 \times LW^2 \quad (1)$$

where L refers to the long diameter of the tumor. W means the short diameter of the tumor. After 13 days of administration, all group mice ($n = 6$) were sacrificed. Other mice for each group ($n = 6$) were further used to evaluate the lifetime.

2.19. M1 and M2 macrophage content of the CT26 tumor by flow cytometry

The tumor of the mice was dissociated into cells by grinding. Then, the cells were incubated with antibodies for APC anti-mouse CD206, KIRAVIA Blue 520 anti-mouse F4/80, PE anti-mouse CD86, and Brilliant Violet 421 anti-mouse CD11b for 2 h at room temperature. Subsequently, flow cytometry was used to detect the content of M1 and M2 macrophages in the tumor by analyzing the fluorescence signal.

2.20. Immunofluorescent staining of GPX4, M1, and M2 markers and HE staining and TUNEL staining

The slices of the tumor, heart, liver, spleen, lungs, and kidney of the mice were stained by HE staining. Moreover, the slices of tumor of the mice were stained by TUNEL staining. Subsequently, the image of HE and TUNEL staining were observed by

microscope and THI (TUNEL, λ_{ex} = 488 nm). The expression of the GPX4, M1, and M2 markers in tumors was performed by immunofluorescent staining. The slices of tumor were separately incubated with GPX4 antibody, INOS antibody, F4/80 antibody, and CD206 antibody for 12 h. After that, the slices were further incubated with various second antibody for 1 h and DAPI for 5 min, then the immunofluorescent images were performed by THI (FITC, λ_{ex} = 488 nm; TRITC, λ_{ex} = 530 nm; DAPI, λ_{ex} = 405 nm).

2.21. *Statistical analysis*

Measurement data were presented as means ± standard deviation (SD). The Student's *t*-test was used to analyze the experimental results through Graph Pad Prism 7.0 software. $P < 0.05$ was identified as statistically significant. $^{*}P < 0.05$; $^{**}P < 0.01$; $^{***}P < 0.001$.

3. Results and discussion

3.1. *Preparation and characterization of nano prodrug*

The Ce6−Pt(IV) was prepared by improving the method reported in the literature[29], and characterized using analytical, NMR, ESI-HRMS, and reversed-phase HPLC (RP-HPLC) (Supporting Information Figs. S1−S4). The obtained Ce6−Pt(IV) was conjugated to P1-mPEG (NP) (Supporting Information Fig. S5). Subsequently, the coordination of Fe^{3+} and gallic acid (GA) with NP led to the formation of NP-G-Fe nanoparticles, with the weight ratios of Fe/Ce6−Pt and Fe/GA being 1:1 and 1:2, respectively (Supporting Information Fig. S6). Based on the dynamic light scattering, the hydrodynamic diameter for NP and NP-G-Fe was 198 and 200 nm, respectively (Supporting Information Fig. S7A and S7B). The zeta potential of the NP-G-Fe remains positive, ranging between 30 and 40 mV due to the remaining cationic residues from polyaspartamine (Fig. S7C). To neutralize the positive surface charge, the nano prodrug was complexed with anionic mPEG-CS to form NPS-G-Fe[30]. By adjusting the initial weight ratio of mPEG-CS to NP-G-Fe, the optimized formulation of NPS-G-Fe suspensions was achieved at a weight ratio of 6 with neutral charged (Fig. S7C), accompanied by a decrease in the nanoparticle diameter to 184 nm and a low polydispersity index (PDI) of 0.11 (Fig. 1A). Following analysis of the Ce6−Pt/Fe^{3+}/GA content, the content of the Ce6−Pt/Fe^{3+}/GA (with the weight ratios of 0.9/0.9/1.1) was finally determined in NPS-G-Fe. Moreover, analysis of stability for NPS-G-Fe nanoparticle using dynamic light scattering showed that NPS-G-Fe nanoparticles possess favorable stability in PBS and DMEM-added FBS from Days 1−7 (Supporting Information Fig. S8). The diameter of NPS-G-Fe was further validated by transmission electron microscopy (TEM) analysis with an approximate particle size of 190 nm (Fig. 1B). Moreover, NPS-G-Fe samples were subjected to elemental mapping using TEM coupled with energy-dispersive X-ray spectroscopy to visualize the composition of the elements, demonstrating a uniform distribution of Pt, Fe, S, N, O, and C elements within the NPS-G-Fe particles (Fig. 1C).

To investigate the efficacy of dual-lock strategy within NPS-G-Fe, the presence of Ce6−Pt(IV), Fe^{3+}, and GA within the NPS-G-Fe particle was measured by UV−Vis absorption peaks (Fig. 1D). Upon 30 min of radiation exposure, slight changes were observed in the absorption peaks of 400 nm and 660 nm in NPS-G-Fe compare to obvious alterations in the 296 nm peak and minor changes in the 400 and 660 nm peaks were shown in NPS-G-Fe treated with acid conditions without radiation, confirming dissociation of metallo-locking. Notably, the decreasing absorption intensities in NPS-G-Fe in an acidic environment were observed after light exposure. This reduction can be attributed to the photodynamic capability of Ce6 being restored following the unlocking of metallo dissociation. Moreover, the fluorescence spectra of NPS-G-Fe showed that the fluorescence of Ce6 in the NPS-G-Fe was diminished due to the quenching effect induced by Fe locking and significantly restored after treating with acid, leading to the dissociation of Fe and unlocking of the framework of nanoparticles (Fig. 1E). Interestingly, the restored fluorescence intensity at 408 nm and 650 nm of the NPS-G-Fe were reduced upon radiation exposure, implying that the formation of the Ce6−Pt(IV) frameworks within the NPS-G-Fe induces photodynamic blenching after iron unlocking. Compared to NPS-G-Fe, a significant fluorescence intensity for the Ce6 of 408 nm and 650 nm was observed in NPS (Supporting Information Fig. S9). Furthermore, the infrared spectra of NPS-G-Fe revealed the presence of two prominent carboxylate bands (COO−, 1670 and 1430 cm^{-1}) corresponding to the linker of the Ce6−Pt(IV) framework that was coordinated with Fe^{3+} (Fig. 1F). This suggests that the NPS-G-Fe particle featured coordination of Ce6−Pt(IV) with Fe^{3+}. The OH stretching vibration band of the GA-based NPS-G-Fe particle was observed to shift from 3275 cm^{-1} to 3515 cm^{-1}, indicating the coordinating of Fe^{3+} to the NPS-G-Fe through intermolecular hydrogen bonding with GA. Additionally, the carboxylic stretching band (C=O, 1715 cm^{-1}) of Ce6−Pt(IV) within the NPS-G-Fe was detected exclusively in samples treated with acidic conditions but not in those treated with radiation exposure, suggesting that the pH-depended dissociation of the Fe^{3+} within the NPS-G-Fe. Besides, the XPS analysis of NPS-G-Fe revealed the presence of two binding energy peaks at 79.5 eV and 76.2 eV, which were indicative of the presence of Pt(IV) (Fig. 1G). Following 20 min of radiation exposure, a slight reduction of the binding energy peaks at 79.5 eV was observed in the NPS-G-Fe. In contrast, the complete elimination of the binding energy peaks at 79.5 eV and the emergence of new binding energy peaks at 72.2 eV were observed in the NPS-G-Fe particle upon exposure at pH 5.5 and subsequent 10 min of radiation. Importantly, density functional theory (DFT) calculations of the Fe−Pt bimetallic complex showed that the fluorescence quenching of the photosensitizer upon complexation with Fe is likely a result of electron transfer from the photosensitizer to the iron ion center. Simultaneously, this circumstance also inhibits light-driven electron transfer from the photosensitizer to the Pt(IV) center (Supporting Information Fig. S10). This suggests that the photoreduction of Pt(IV) to Pt(II) within the NPS-G-Fe occurred preferentially, leading to the formation of Pt(II)-based species with a lower binding energy. Subsequently, the release of Pt and Fe content within the NPS-G-Fe was investigated using inductively coupled plasma mass spectrometry (ICP-MS). As shown in Fig. 1H, the ICP-MS analysis of the NPS-G-Fe particle following 20 min of radiation exposure revealed a Pt content of 30% of releasing. In contrast, a significant release of Pt content (80%) was observed in the NPS-G-Fe particle treatment with acid (pH 5.5) and subsequent 10 min of radiation, indicating that faster release of Pt from the NPS-G-Fe under acidic conditions with radiation treatment. Moreover, similar release rates of Fe within the NPS-G-Fe were also observed in treating with acid conditions. After

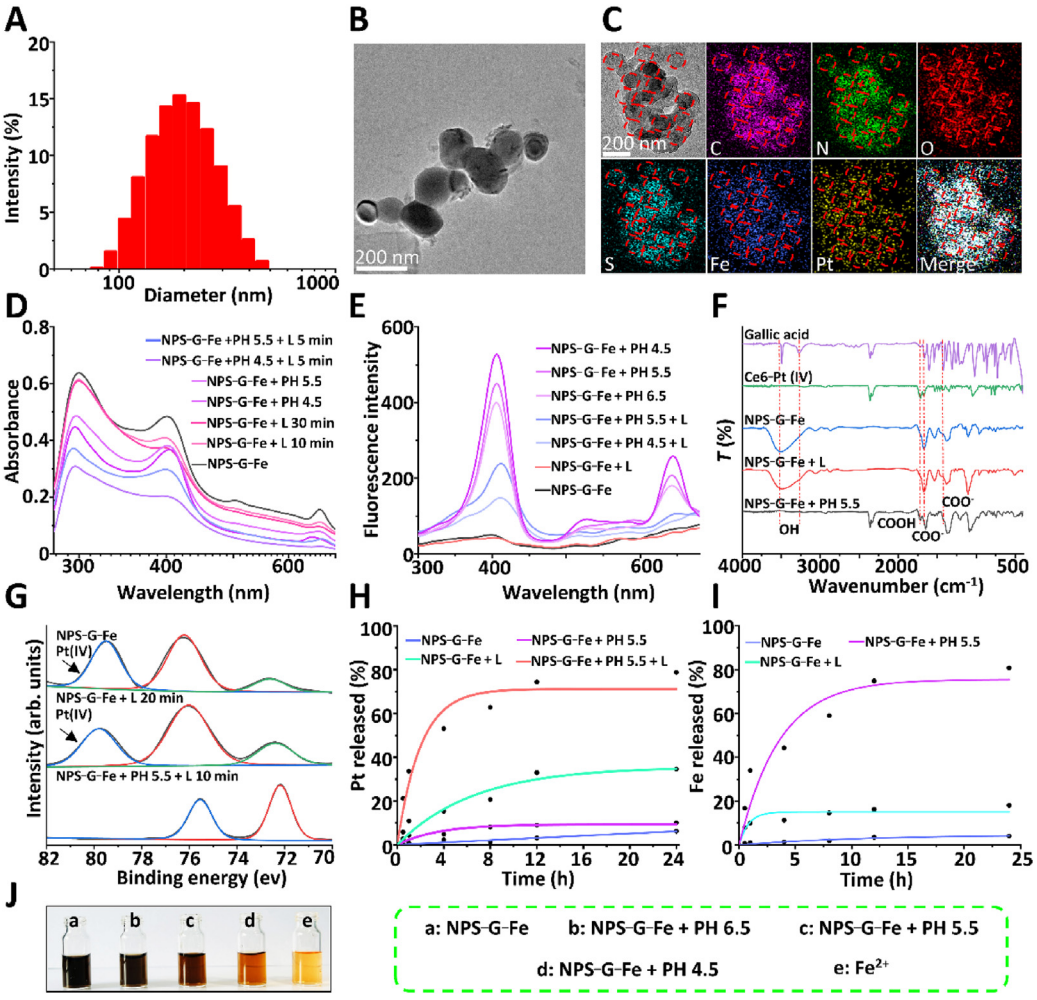

Figure 1 Characterization and photophysical properties of NPS-G-Fe. (A) Dynamic light scattering spectrum. (B) Transmission electron microscopy image (scale bar = 200 nm). (C) Elemental mapping of transmission electron microscopy image using coupling to energy-dispersive X-ray spectroscopy (scale bar = 200 nm). (D) UV−Vis spectroscopy of NPS-G-Fe in various conditions. (E) Fluorescence spectroscopy of NPS-G-Fe in various conditions. (F) Infrared spectroscopy of Ce6−Pt (IV), GA, NPS-G-Fe under radiation for 10 min (with a 660 nm laser, 0.8 W/cm^2, 5 min) or acid condition. (G) X-ray photoelectron spectrum of NPS-G-Fe in the dark, radiation for 20 min, or acid condition with radiation for 10 min. (H) Release of Pt for NPS-G-Fe in the dark, radiation for 20 min, acid condition, or acid condition with radiation for 10 min. (I) Release of Fe for NPS-G-Fe in the dark, radiation for 20 min, or acid condition. (J) *O*-Phenanthroline chromogenic of Fe^{2+} or Fe^3 in NPS-G-Fe in the dark and various acid conditions.

20 min of radiation with the NPS-G-Fe, the release of Fe content (10%) was detected by ICP-MS. In contrast, a significant release of Fe content (80%) was observed in the NPS-G-Fe particle treatment with acid (PH 5.5), indicating that faster release of Fe from the NPS-G-Fe under acidic conditions (Fig. 1I). Additionally, *O*-phenanthroline was utilized to identify the presence of Fe^{3+} or Fe^{2+} within the NPS-G-Fe particle, and the resulting color change was observed to assess the impact of the reduction of Fe^{3+} to Fe^{2+} by GA. As illustrated in Fig. 1J, a strong conversion of Fe^{3+} to Fe^{2+} was observed under acid-dependent conditions for the NPS-G-Fe, indicating that GA selectively triggers the reduction of Fe^{3+} to Fe^{2+} within the NPS-G-Fe particle under acidic conditions. Taking together, these results align with previous research demonstrating the dual-lock ability of NPS-G-Fe to selectively activate photoactivated Pt(IV) prodrugs in specific environmental conditions.

3.2. *Cytotoxicity induced by nano prodrug*

The *in vitro* biological effects of various Pt-containing compounds were assessed on various cell lines. Firstly, we evaluate the combination index (CI) value of chemotherapy and photodynamic therapy. The Ce6−Pt(IV) constituted by Ce6 and oxaliplatin (ratio of 1:1) was used to evaluate combination index (CI) values. The result of Table S1 showed that a synergism effect (CI < 1) was observed in Ce6−Pt(IV) from ED50 to ED95, which indicated that the combination of Ce6 and oxaliplatin (Ce6−Pt(IV)) was a synergism effect (Supporting Information Table S1). As shown in Fig. 2A−C, the formulations with light irradiation exhibited greater toxicity compared to those without irradiation. Following 48 h incubation after radiation, functionalized NPS-G-Fe demonstrated remarkable cytotoxicity upon irradiation with the IC50 values of 0.2, 0.6, and 0.27 μmol/L for CT26, 4T1, and

HCT116 cells, respectively, which is much lower than the IC_{50} presented by the NPS in same cell lines with radiation. Meanwhile, NPS also exhibited enhanced antitumor cytotoxicity compared to Ce6−Pt(IV) under the radiation, as indicated by the IC_{50} values of 0.53 μmol/L *vs.* 1.06 μmol/L, 0.84 μmol/L *vs.* 2.05 μmol/L, and 0.52 μmol/L *vs.* 1.42 μmol/L for CT26, 4T1, and HCT116 cells, respectively. Furthermore, the therapeutic effects of various Pt-containing compounds were evaluated in the 3D multicellular cancer spheroids (MCSs) using optical microscopy. The result of volume change of 3D MCSs on Days 1, 2, 3, 4, 5, 6, and 7 showed that the NPS-G-Fe upon irradiation presented the greater inhibiting grow effect of the 3D MCSs, compared to NPS upon irradiation or Ce6−Pt(IV) upon irradiation or oxaliplatin (Supporting Information Fig. S11). These findings suggest that the dual-lock metallo-nano prodrug significantly enhances antitumor cytotoxicity, especially under radiation conditions. Moreover, the toxicity of various Pt-containing compounds was assessed on HUVECs and raw cells. Following 48 h incubating after radiation or without irradiation, various Pt-containing compounds demonstrated low toxicity in HUVECs and raw cells, compared to the cancer cells (Supporting Information Fig. S12). The enhanced antitumor effect of nano prodrug was further evaluated through flow cytometry. In comparison with oxaliplatin, apoptotic effects were increased by 4.6-, 5.7-, and 6.8-fold (Fig. 2D and E) for Ce6−Pt(IV), NPS, and NPS-G-Fe after irradiation, respectively. Moreover, the therapeutic effects on CT26 cells were evaluated using live/dead staining and Thunder high-resolution imaging system (THINDER). The decreasing green fluorescence (Calcein AM) and increasing red fluorescence (PI) of cells treated by NPS-G-Fe demonstrated that metallo-nano prodrug exhibited minimal live cells compared to Ce6−Pt(IV) and NPS in the same condition (Fig. 2F). These findings provide further evidence of the significant therapeutic effects of dual-locked NPS-G-Fe, highlighting its potential as a promising therapeutic strategy.

3.3. *Biological mechanisms of nano prodrug in vitro*

The cellular endocytosis of photosensitizer and generation of reactive oxygen species (ROS) is a crucial process in effective photodynamic therapy[31]. To investigate the underlying biological mechanisms, cellular uptake and ROS production of Ce6−Pt(IV), NPS, and NPS-G-Fe were observed using the THI and flow cytometry. As shown in Fig. 3A−E, upon treatment with or without irradiation for 4 h, both NPS and NPS-G-Fe significantly increased the uptake of Ce6 and ROS content in comparison to Ce6−Pt(IV), suggesting that the nanoparticles promoted the uptake of Ce6 and ROS generation. Notably, the treatment of NPS-G-Fe upon irradiation or without irradiation was found to result in a higher uptake of Ce6 and ROS content than the treatment of NPS upon irradiation or without irradiation. Moreover, the cellular uptake analysis revealed noticeable differences in the uptake of NPS and NPS-G-Fe compared to NP and NP-G-Fe, indicating that CS within NPS-G-Fe contributes to an improved tumor-targeting effect. Subsequently, the cellular uptake of Pt in CT26 cells exposed to various formulations was analyzed using ICP-MS. As shown in Fig. 3F, after 4 h treatment, the cellular content of Pt for Ce6−Pt(IV), NPS, and NPS-G-Fe was 1.5, 3.2, and 4.2 times higher than that observed with oxaliplatin, respectively. The findings were consistent with those from the cellular uptake analysis of Ce6 fluorescence, revealing that NPS-G-Fe resulted in a higher cellular uptake compared to NPS. Platinum drugs enter tumor cells and form cross-linked products with DNA, leading to distortion of the DNA double helix, inhibition of replication, and ultimately inducing DNA double-strand breaks and cell apoptosis[32]. To measure the efficacy of Pt-DNA crosslinking in the NPS-G-Fe, the cellular DNA-Pt adducts of CT26 cells exposed to oxaliplatin, NPS, and NPS-G-Fe were analyzed. As shown in Fig. 3G, a higher amount of Pt-DNA adducts was measured following irradiation for 4 h in the treatment of NPS and NPS-G-Fe, with NPS-G-Fe exhibiting the highest capacity for DNA-Pt adducts. Interestingly, compared to oxaliplatin, a significant increase in Pt-DNA adducts was observed in the treatment of NPS upon irradiation (10.4-fold increase), and an even higher increase was noted in the treatment of NPS-G-Fe upon irradiation (13-fold increase) (Fig. 3G). These results indicated that the functionalized NPS-G-Fe particle promoted the cellular uptake of nanoparticles, had the potential for ROS generation and inhibited cell division by forming harmful Pt-DNA adducts, which was further enhanced upon exposure to irradiation and contributed to its enhanced cytotoxicity.

The reduction of intracellular GSH levels enhances the anticancer efficacy of platinum-based chemotherapy[33]. Thus, the intracellular GSH of CT26 cells treated with different Pt-compounds was measured. The results showed that the content of GSH was reduced by 1.1 times (NPS) and 1.3 times (NPS-G-Fe) in the absence of irradiation and was further decreased by 1.9 times (NPS) and 2.7 times (NPS-G-Fe) upon irradiation (Fig. 3H). In addition to intracellular GSH levels, dissociation of Fe^{2+} from NP-G-Fe is also featured for ferroptosis and improves anticancer efficacy PDT[28]. Analysis of cellular Fe^{2+} content revealed a considerable amount of Fe^{2+} generated in NPS-G-Fe, which was approximately 2.6-fold higher than that observed in the treatment of NPS without irradiation, due to GA within NPS-G-Fe initiated conversion of Fe^{3+} into Fe^{2+} in CT26 tumor cells (Fig. 3I). Additionally, a significant increase in Fe^{2+} content was observed in the treatment of NPS-G-Fe upon irradiation, where the level of Fe^{2+} was elevated by 2.8-fold compared to the treatment of NPS with irradiation (Fig. 3I). Triggering ferroptosis effect improves anticancer efficacy PDT by increasing ROS levels and decreasing intracellular GSH content[28]. Therefore, the improvement in the biological effects of cellular ROS and Pt-DNA crosslinking in the treatment of NPS-G-Fe with irradiation, compared to NPS upon irradiation, may be attributed to the ferroptosis of cancer cells. To confirm this hypothesis, a Western blot analysis of GPX4 protein in CT26 cells was performed. GPX4 protein acts as a crucial regulator of ferroptosis[34]. As shown in Fig. 3J and K, NPS-G-Fe with irradiation led to a tremendous decrease in the expression level of GPX4, indicating that the GPX4-mediated ferroptosis pathway could be triggered by photoactivated NPS-G-Fe (Fig. 3J and K). Thus, the treatment of dual-locked metallo-nano prodrug with irradiation increased intracellular ROS and Fe^{2+} levels, and reduced the GSH content in CT26 cells, which was found to induce ferroptosis, and boosted the efficacy of photodynamic therapy and photoactivated chemotherapy.

3.4. *Macrophage polarization induced by nano prodrug in vitro*

PDT synergized with ferroptosis has been shown to activate and enlarge the polarization of tumor-associated macrophages, to inhibit tumor growth[28,35]. To investigate macrophage polarization induced by metallo-nano prodrugs, raw macrophages (M0 macrophage) separately exposed to a supernatants medium extracted from CT26 cells after treatment with various formulations, and the gene expression relating to macrophage polarization

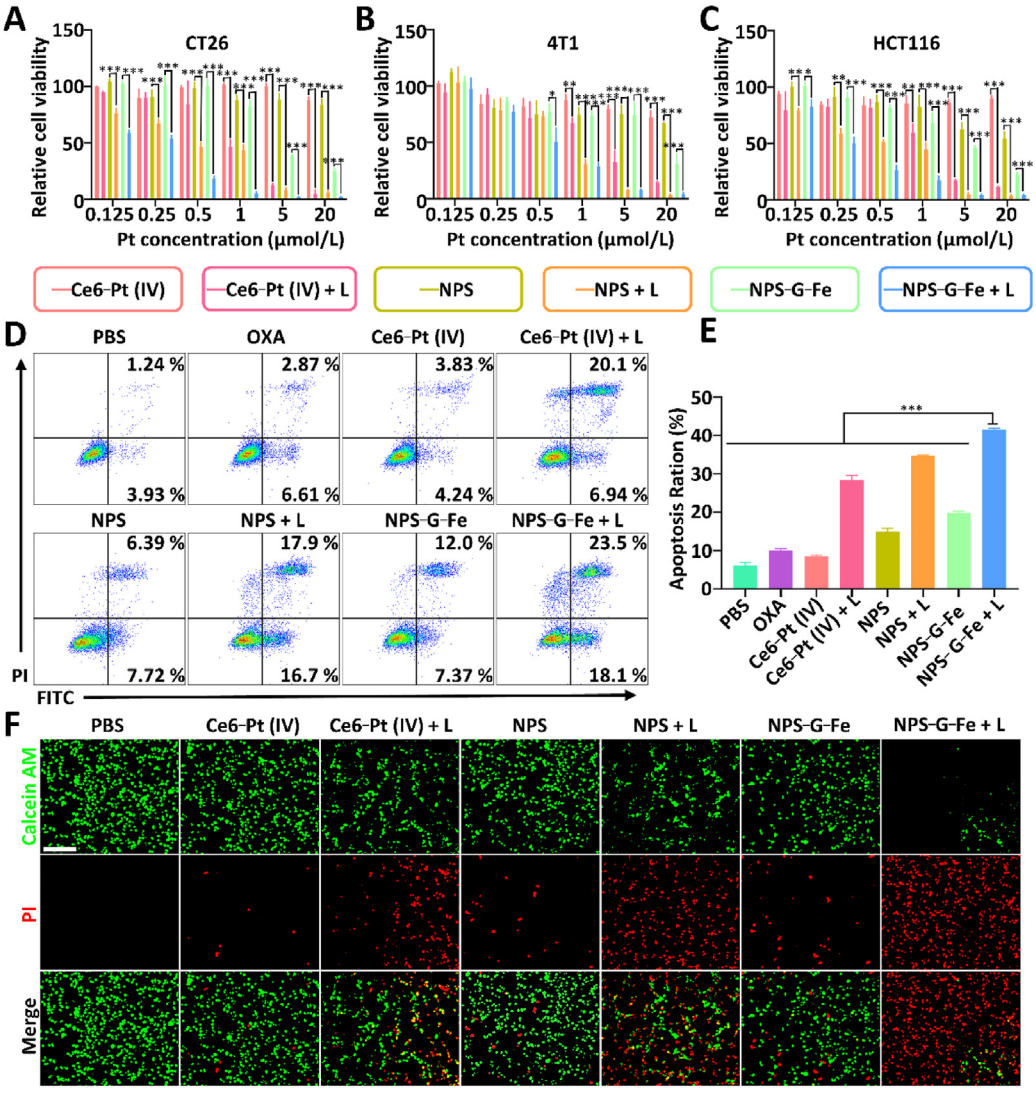

Figure 2 Cytotoxic effect in CT26, 4T1, and HCT116 cells and apoptosis effect in CT26 cells. (A) Cell viability of CT26 cells with various Pt-containing compounds and exposure to irradiation (660 nm, 0.8 W/cm^2, 5 min) or dark. (B) Cell viability of 4T1 cells with various Pt-containing compounds and exposure to irradiation 5 min or dark. (C) Cell viability of HCT116 cells with various Pt-containing compounds and exposure to irradiation 5 min or dark. (D) Flow cytometry for CT26 cells apoptosis treating with various Pt-containing compounds exposure to irradiation 5 min or dark. (E) Quantitative analysis of the CT26 cells apoptosis ratio. (F) Live/dead staining of CT26 cells treated with various Pt-containing compounds exposure to irradiation 5 min or dark, green (Calcein AM, live cells), red (PI, dead cells). Scale bar = 400 μm. Data are presented as mean ± SD (n = 3). *P < 0.05; **P < 0.01; ***P < 0.001.

such as *Inos* (M1) and *Arg1* (M2) were analyzed using PCR (Fig. 4A). The results showed that *Inos* was significantly increased by 23.2- and 35.7-fold in response to the supernatant medium from NPS and NPS-G-Fe with irradiation, while *Arg1* was reduced by 2.5-and 9.5-fold in response to the supernatant medium from NPS and NPS-G-Fe with irradiation, compared to PBS control (Fig. 4B and C). M2 macrophages induced by IL-4 (50 ng/mL) also was used as control to evaluate polarization effect induced by NPS and NPS-G-Fe (Fig. 4D). The PCR analysis of gene expression related to polarization showed that the expression of *Inos* was upregulated by 1.9- and 3.3-fold in response to NPS and NPS-G-Fe with irradiation, compared to M2 macrophages (Fig. 4E). Conversely, the expression *Arg1* was downregulated by 1.8- and 2.1-fold in response to NPS and NPS-G-Fe with irradiation, compared to M2 macrophages (Fig. 4F). To further validate the effect of macrophage polarization induced by NPS and NPS-G-Fe, immunofluorescent staining, quantitative cytometry, and the content of TNF-α in M2 macrophages were used to further to verify. The results for immunofluorescent staining showed that the higher M1 polarization NPS-G-Fe with irradiation was found than that observed with NPS with irradiation by a decrease in the expression of CD206 and an increase in the expression of INOS in the M2 macrophages exposed to supernatant media from CT26 cells (Fig. 4H). Moreover, the result for quantitative cytometry showed that a 1.6-fold decrease in the content of M2 macrophages and a 7.6-fold increase in the content of M1 macrophages were observed in response to NPS-G-Fe combined with irradiation, compared to M2 macrophages

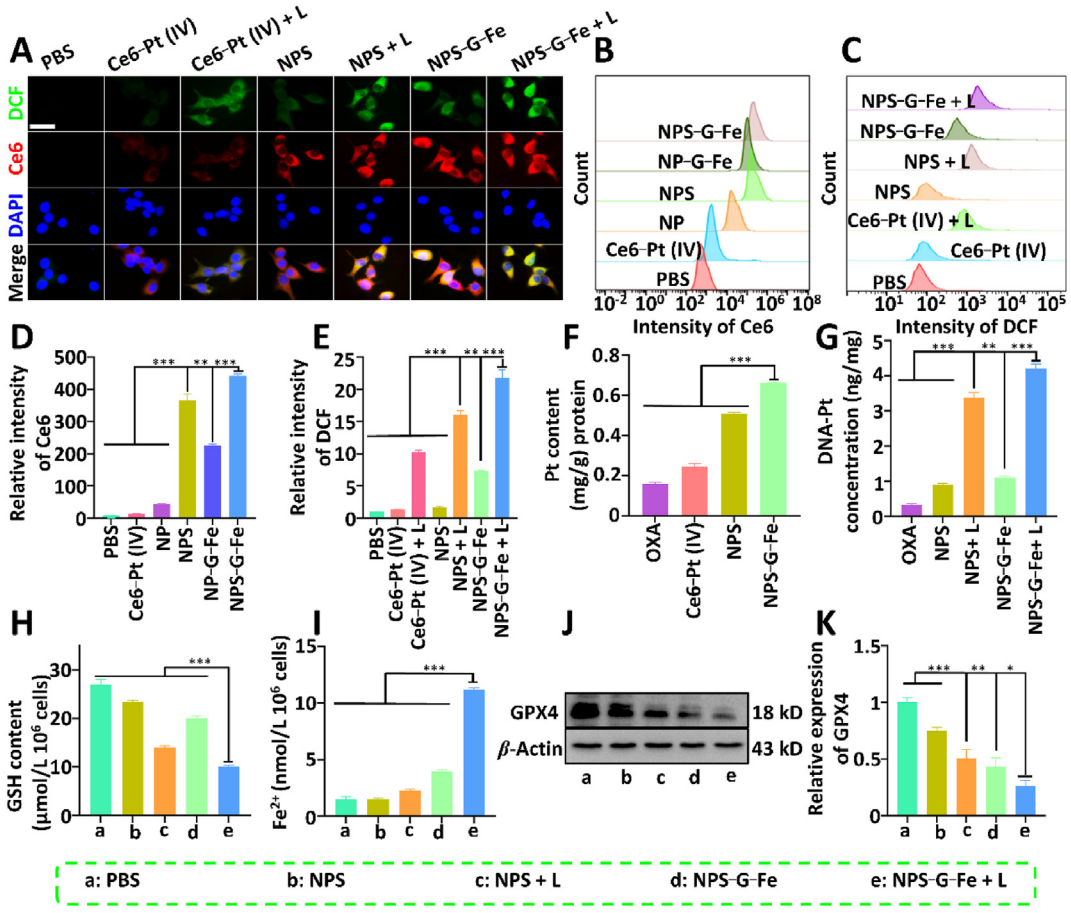

Figure 3 CT26 cellular uptake, ROS generation, Pt-DNA crosslinking, and ferroptosis effect. (A) Uptake and ROS fluorescence images of CT26 cells with various Pt-containing compounds exposure to irradiation (660 nm, 0.8 W/cm^2, 5 min) or dark, red (Ce6), green (DCFH-DA, ROS), blue (DAPI). Scale bar = 100 μm. (B) Image of Ce6 fluorescence intensity in CT26 cells with various Pt-containing compounds after 4 h using flow cytometry. (C) Image of DCF fluorescence intensity in CT26 cells with various Pt-containing compounds exposed to irradiation for 5 min or dark using flow cytometry. (D) Relative B, quantitative analysis content of Ce6 fluorescence intensity in CT26 cells. (E) Relative C, quantitative analysis content of DCF fluorescence intensity in CT26 cells. (F) Pt content of CT26 cells with various Pt-containing compounds for 4 h. (G) Relative content of Pt-DNA of CT26 cells with various Pt-containing compounds for 4 h and exposure to irradiation 5 min or dark. (H) Relative content of GSH of CT26 cells with various Pt-containing compounds for 4 h and exposure to irradiation 5 min or dark. (I) Relative content of Fe^{2+} of CT26 cells with various Pt-containing compounds for 4 h and exposure to irradiation 5 min or dark. (J) Western blot image of GPX4 of CT26 cells with various Pt-containing compounds exposure to irradiation 5 min or dark. (K) Relative J, quantitative analysis of GPX4 protein expression (fold of normal) in CT26 cells. Data are presented as mean ± SD (n = 3). *P < 0.05; **P < 0.01; ***P < 0.001.

(Fig. 4G–I, and J). As shown in Fig. 4K, the cell supernatant content of TNF-α was evaluated at a 3.98-fold increase in response to NPS-G-Fe combined with irradiation, compared to M2 macrophages. These findings provide further evidence that NPS-G-Fe with irradiation promotes macrophage polarization towards an M1 phenotype and suppresses the polarization towards an M2 phenotype.

3.5. *Biodistribution and anti-tumor efficacy of nano prodrug*

Subsequently, tumor-targeting and tumor-inhibiting effects of various formulations were performed in the CT26 colorectal cancer model (Fig. 5A). To explore the biodistribution in the CT26 colorectal cancer model, the NPS-G-Fe was labeled with the fluorophore IR780 to achieve the fluorescent nanoparticle (FNPS-G-Fe). The result for hydrodynamic diameter showed the hydrodynamic diameter of FNPS-G-Fe was 178 nm, compared with NPS-G-Fe (184 nm) (Supporting Information Fig. S13). Thus, based on the change in hydrodynamic diameter IR780 labeling does not affect the nanoparticles. The biodistribution of nano-prodrug was performed, where the fluorescent was observed to accumulate in the tumor site, which was almost similar for the liver both *in vivo* and *ex vivo* after administration FNPS-G-Fe *via* tail veins (Fig. 5B and C). The results of biodistribution demonstrated an enhanced targeting effect in tumors when treated with FNPS-G-Fe in comparison to FNP-G-Fe (Fig. 5B). Pharmacokinetic experiment was further used to evaluate the features in blood circulation for NPS-G-Fe. Following a single intravenous (i.v.) injection, functionalized NPS-G-Fe demonstrated remarkable circulation half-life in blood vessels with the 81.8 h, compared to Ce6–Pt(IV) with 0.93 h and NP-G-Fe with 0.64 h (Supporting Information Fig. S14). This provides additional evidence that CS within NPS-G-Fe contributes to an improved time in blood circulation and tumor-targeting effect. Simultaneously, Pt and Fe content

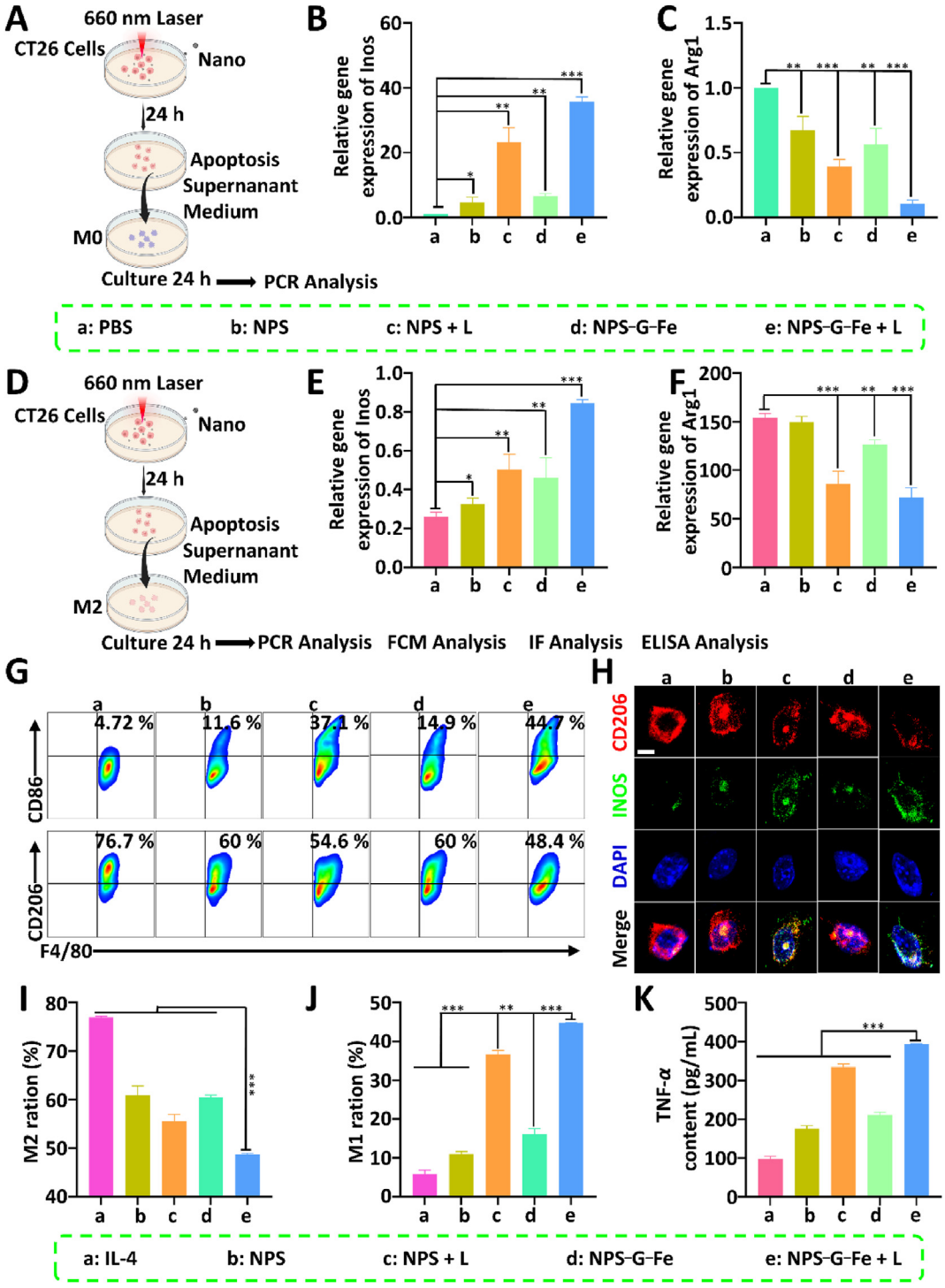

Figure 4 Macrophage polarization effect. (A) Diagram for M0 macrophage polarization effect for various apoptosis supernatants of culture medium for CT26 cells. (B) Relative gene expression of *Inos* of M0 macrophages treated with various apoptosis supernatants of culture medium for CT26 cells for 24 h. (C) Relative gene expression of *Arg1* of M0 macrophages treated with various apoptosis supernatants of culture medium for CT26 cells for 24 h. (D) Diagram for M2 macrophage polarization effect for various apoptosis supernatants of culture medium for CT26 cells. (E) Relative gene expression of *Inos* of raw macrophage (M2) treated with various apoptosis supernatants of culture medium for CT26 cells for 24 h. (F) Relative gene expression of *Arg1* of raw macrophages (M2) treated with various apoptosis supernatants of culture medium for CT26 cells for 24 h. (G) Image of flow cytometry of the M1 and M2 macrophages of raw cells using flow cytometry. (H) Immunofluorescent staining of CD206 and INOS for raw macrophages (M2) treated with various apoptosis supernatants of culture medium for CT26 cells for 24 h, red (CD206), green (INOS), blue (DAPI). Scale bar = 25 μm. (I) Relative G, quantitative content of M2 rations of the raw cells. (J) Relative G, quantitative content of M1 rations of the raw cells. (K) Quantitative analysis of TNF-α content in raw cell supernatant using ELISA. Data are presented as mean ± SD ($n = 3$). *$P < 0.05$; **$P < 0.01$; ***$P < 0.001$.

accumulating in organs and tumors were analyzed. The results demonstrated the amount of Pt and Fe in the tumor was 1.5-fold or 1.2-fold higher in comparison to that of the liver, while less content of Pt and Fe was detected in the other organs (Fig. 5D−E). Tumor inhibition of various formulations was further evaluated in CT26 colorectal cancer models. As shown in Fig. 5F, NPS-G-Fe in irradiation exhibited the highest tumor suppression and eradicated tumor volume compared to NPS and Ce6−Pt(IV) with irradiation (Supporting Information Fig. S15). While treating with oxaliplatin, Ce6−Pt(IV), and NPS without irradiation was a slight reduction in the tumor volume (Fig. 5F and Fig. S15). Consistent with the effect of inhibiting tumor growth, the weight of tumor also was reduced to varying degrees after treatment of the various formulations (Fig. 5I). Furthermore, the recording of body weight of tumor-bearing mice showed that no body weight loss and behavioral abnormalities were observed during the treatment (Fig. 5G). The survival rate of tumor-bearing mice with irradiation or without irradiation was evaluated. A relatively extended survival rate for the animals treated with Ce6−Pt(IV) and NPS (with irradiation or without irradiation) and NPS-G-Fe (without irradiation) was observed compared with oxaliplatin. Notably, continuous observation of post-treatment outcomes revealed that 83% of the animals treated with NPS-G-Fe combined with irradiation were still alive after Day 30, whereas all animals treated with

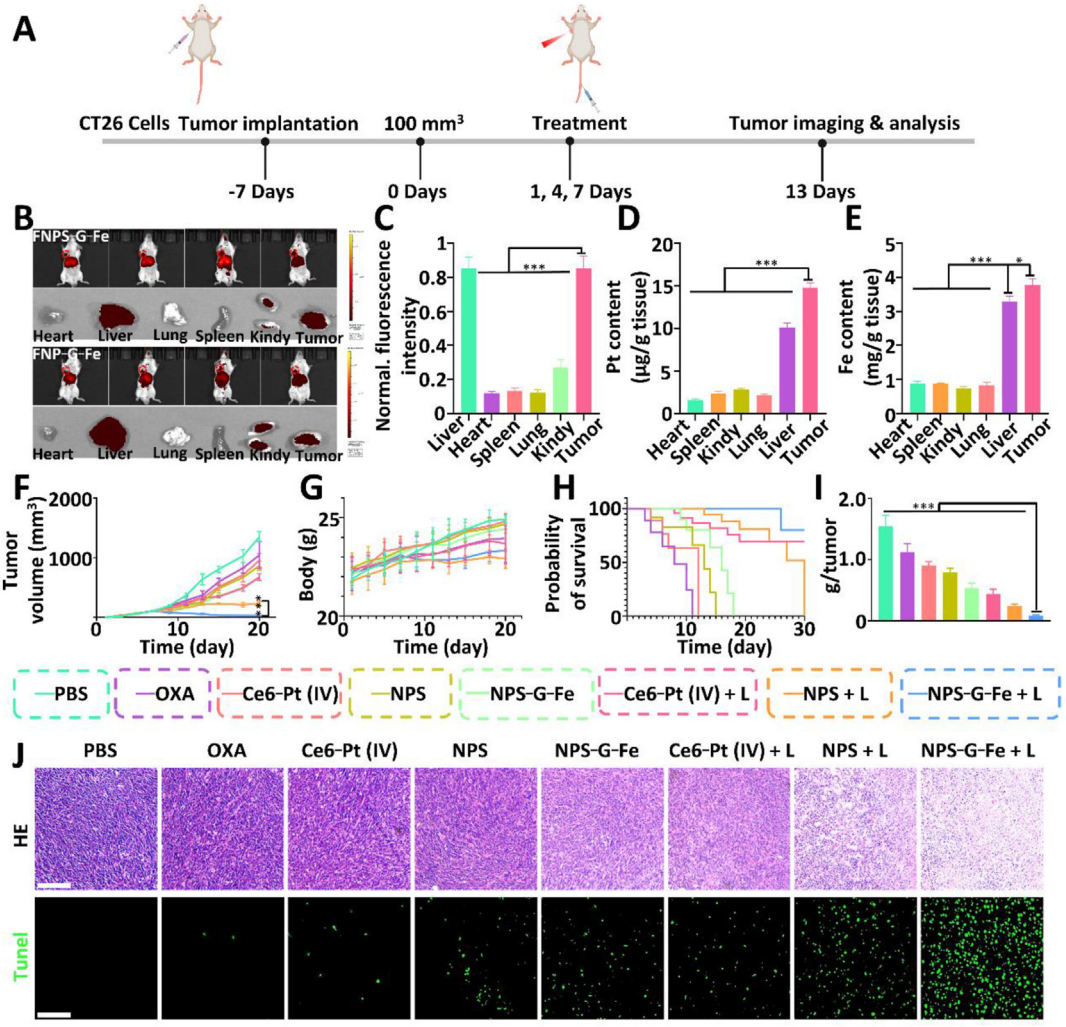

Figure 5 Biodistribution, tumor growth inhibition, and survival for treatment of the CT26-tumor mice. (A) Diagram for establishment and evaluation of the therapeutic effect of CT26 colorectal cancer model. (B) Biodistribution of FNPS-G-Fe (above) and FNP-G-Fe (below) for body, tumor, and major organ (after sacrifice) of the CT26 colorectal cancer model using IVIS. (C) Related to B, quantitative analysis of the IR780 fluorescence of the FNPS-G-Fe for tumor, and major organ (after sacrifice) of the CT26 colorectal cancer model. Data are presented as mean ± SD ($n = 3$). (D) Pt content of tumor and major organ of the CT26 colorectal cancer model detected by ICP-MS. Data are presented as mean ± SD ($n = 3$). (E) Fe content of tumor and major organ of the CT26 colorectal cancer model detected by ICP-MS. Data are presented as mean ± SD ($n = 3$). (F) Growing curves of tumors of CT26 colorectal cancer model treated by various formulations exposure to irradiation (660 nm, 0.8 W/cm^2, 5 min) or dark. Data are presented as mean ± SD ($n = 6$). (G) Body weight curves of the CT26 colorectal cancer model treated by various formulations exposure to irradiation 5 min or dark. Data are presented as mean ± SD ($n = 6$). (H) Survival curve of the CT26 colorectal cancer mode after treatment for day 30. Data are presented as mean ± SD ($n = 6$). (I) Tumor weight of the CT26 colorectal cancer model after sacrifice. Data are presented as mean ± SD ($n = 6$). (J) HE or TUNEL staining of the tumor tissues after sacrifice. Scale bar = 400 μm *$P < 0.05$; **$P < 0.01$; ***$P < 0.001$.

other formulations had died due to recurrent tumor growth (Fig. 5H). Subsequently, a comprehensive analysis of the tumors and tissues of the treated animals was conducted using hematoxylin and eosin (HE) staining and TUNEL fluorescence staining. The results revealed remarkable nuclear fragmentation and nucleolytic activity (HE staining) as well as apoptosis (TUNEL staining) in the subjects treated with NPS-G-Fe in combination with irradiation, which was notably absent in the subjects treated with other formulations (Fig. 5J). Additionally, HE staining for key organs and hematological assessments conducted on the dosed animals confirmed the non-toxicity of the various formulations administered (Supporting Information Figs. S16 and S17). These results corroborate the notion that the dual-lock metallo-nano-prodrug possesses exceptional tumor-targeting capabilities, a favorable safety profile, and substantial therapeutic potential.

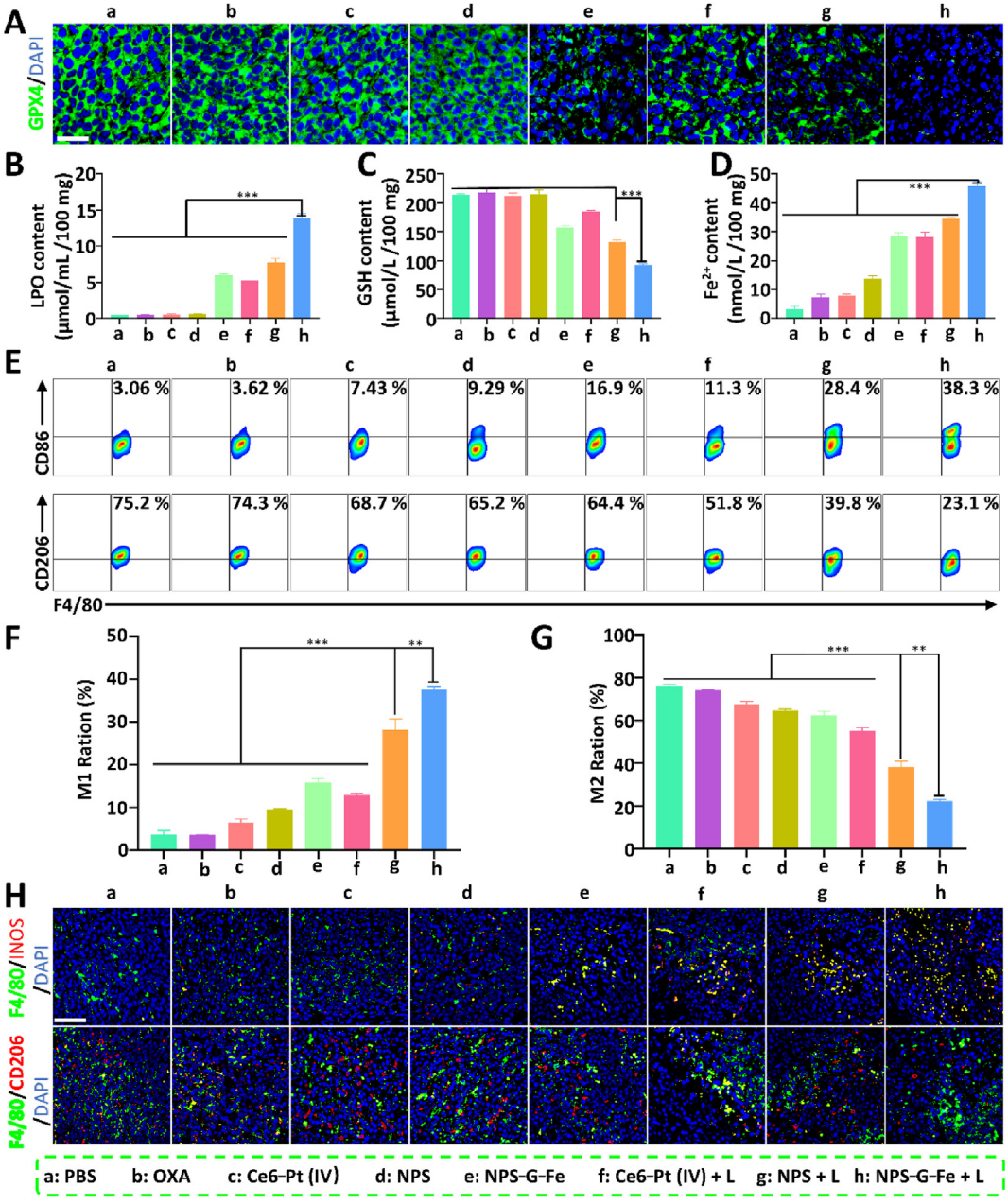

Figure 6 Evaluation of ferroptosis and macrophage polarization of the tumor for treatment of the CT26-tumor mice. (A) Immunofluorescent staining of GPX4 of the tumor of the CT26-tumor mice after sacrificed, green (GPX4), blue (DAPI), scale bar = 100 μm. (B) Quantitative analysis of LPO content of the tumor of the CT26-tumor mice. (C) Quantitative analysis of GSH content of the tumor of the CT26-tumor mice. (D) Quantitative analysis of Fe^{2+} content of the tumor of the CT26-tumor mice. (E) Image of flow cytometry of the M1 and M2 macrophages of the tumor of the CT26-tumor mice using flow cytometry. (F) Relative E, quantitative content of M1 rations of the CT26-tumor mice. (G) Relative E, quantitative content of M2 rations of the CT26-tumor mice. (H) Immunofluorescent staining of F4/80 and CD206 or F4/80 and INOS of the CT26-tumor mice, green (F4/80), red (CD206), red (INOS), blue (DAPI), scale bar = 200 μm. Data are presented as mean ± SD (n = 3). *P < 0.05; **P < 0.01; ***P < 0.001.

3.6. *Macrophage polarization and ferroptosis initiated by nano prodrug in vivo*

To elucidate the mechanism behind the highly efficient tumor inhibition exhibited by the dual-lock metallo-nano prodrugs, further investigation was conducted on the impact of ferroptosis and macrophage polarization on the tumor in the CT26 colorectal cancer model after treatment with various Pt-containing compounds. As shown in Fig. 6A, the expression of GPX4 in tumors was found to be significantly reduced in response to treatment with NPS-G-Fe combined with irradiation compared to those treated with other Pt-containing compounds, as determined using immunofluorescent staining. Furthermore, the content of Fe^{2+}, GSH, LPO, and MDA in the tumor was also further analyzed to support the ferroptosis induced by NPS-G-Fe. As shown in Fig. 6B−D, and Supporting Information Fig. S18, elevating the content of Fe^{2+}, MDA, and LPO and decreasing GSH in tumor tissues were observed in NPS-G-Fe combined with irradiation compared to those treated with other Pt-containing compounds. To investigate the changes in M1 and M2 macrophages in tumors, flow cytometry, and immunofluorescent staining techniques were utilized. As compared to treatment with oxaliplatin, a 3.3-fold decrease in the content of M2 macrophages and a 10.5-fold increase in the content of M1 macrophages were observed in response to NPS-G-Fe combined with irradiation (Fig. 6E−G). The results obtained from flow cytometry were corroborated by immunofluorescent staining, which demonstrated that the fluorescence of CD206 was significantly reduced and that of INOS was sharply increased in response to NPS-G-Fe combined with irradiation (Fig. 6H). Overall, these results suggest that the combination of NPS-G-Fe and irradiation may enhance the anti-tumor efficacy by inducing ferroptosis and polarizing macrophages towards an M1 phenotype. Overall, both the *in vitro* and *in vivo* results suggest that the dual-lock strategy for constructing Pt(IV)-based formulations could serve as a promising approach for future cancer therapy due to the favorable features of these formulations, such as cooperative activation and high-specificity therapy, to overcome the limitations associated with PDT and chemotherapy.

4. Conclusions

In summary, the sequential dual-lock strategy employed in the development of Pt(IV) nano prodrugs enables their activation by both the acidic tumor microenvironment and red light, thereby enhancing the efficacy of photodynamic and chemotherapy interventions in cancer treatment. This approach involves the preparation of photoactivated Pt(IV) containing nano prodrug (NP), followed by the coordination of Fe^{3+} and GA with the Ce6 in NP to "lock" its photoactivity, and subsequent coating with PEG-CS to produce dual-locked metallo-nano-prodrug. The first lock of NPS-G-Fe is initially triggered by the acidic tumor environment, causing the dissociation of Fe^{3+} and GA from NPS-G-Fe, resulting in the restoration of Ce6 photoactivity. The second lock is unlocked by a red light, activating photodynamic therapy and reducing the Pt(IV) to Pt(II) drugs for chemotherapy. Utilization of this strategy resulted in a significant improvement in the therapeutic effectiveness of NPS-G-Fe, which was primarily attributed to its high intracellular uptake, along with the dissociated GA-induced conversion of Fe^{3+} to Fe^{2+} and depletion of intracellular GSH, leading to ferroptosis induction. The radiation-enhanced potency of NPS-G-Fe treatment had a multiplicative effect on treatment efficacy. Moreover, the significant impact of NPS-G-Fe following radiation on tumor-associated macrophage polarization was confirmed, further enhancing the overall therapeutic outcome. Taken together, the implementation of a sequential dual-locking strategy in the development of photoactivated Pt(IV)-based metallo-nano prodrugs offers a versatile platform for the codelivery of therapeutic agents, exhibiting significant potential for synergistic tumor therapy while minimizing adverse side effects.

Acknowledgments

This work was supported by the Jiangsu Province Postgraduate Research Innovation Program and Jiangsu Province Postgraduate Practice Innovation Program Fund (021093002589, China), National Key Research and Development Program of China (2023YFB3813001) and National Natural Science Foundation of China (52073145). Thanks to technical support for *in vivo* imaging of small animals by Zuoxiu Tie from Nanjing University (Nanjing, China).

Author contributions

Jun Li, Qiang Zhang, Hao Yang, Wenli Lu, Yulong Fu, Yingcai Xiong, Xuan Wang, Tianming Lu, Yanlin Xin, and Zejuan Xie designed and performed chemical, photophysical, DFT calculation, and biological experiments. Jun Li data processed data and wrote the manuscript. Weichao Chen, Guoqiang Wang, Yuanyuan Guo, and Ruogu Qi supervised the work. All authors have approved the final version of this paper.

Conflicts of interest

The authors have no conflicts of interest to declare.

Appendix A. Supporting information

Supporting information to this article can be found online at https://doi.org/10.1016/j.apsb.2024.02.024.

References

1. Wang D, Lippard SJ. Cellular processing of platinum anticancer drugs. *Nat Rev Drug Discov* 2005;**4**:307−20.
2. Kelland L. The resurgence of platinum-based cancer chemotherapy. *Nat Rev Cancer* 2007;**7**:573−84.
3. Johnstone TC, Suntharalingam K, Lippard SJ. The next generation of platinum drugs: targeted Pt(II) agents, nanoparticle delivery, and Pt(IV) prodrugs. *Chem Rev* 2016;**116**:3436−86.
4. Xiao HH, Qi RG, Li T, Awuah SG, Zheng YR, Wei W, et al. Maximizing synergistic activity when combining RNAi and platinum-based anticancer agents. *J Am Chem Soc* 2017;**139**:3033−44.
5. Rautio J, Meanwell NA, Di L, Hageman MJ. The expanding role of prodrugs in contemporary drug design and development. *Nat Rev Drug Discov* 2018;**17**:559−87.
6. Chen HZ, Zeng XW, Tham HP, Phua SZF, Cheng W, Zeng WF, et al. NIR-light-activated combination therapy with a precise ratio of photosensitizer and prodrug using a host-guest strategy. *Angew Chem Int Ed Engl* 2019;**58**:7641−6.
7. Ong JX, Lim CSQ, Le HV, Ang WH. A ratiometric fluorescent probe for cisplatin: Investigating the intracellular reduction of platinum(IV) prodrug complexes. *Angew Chem Int Ed Engl* 2019;**58**:164−7.

8. Yuan SM, Zhu Y, Dai Y, Wang Y, Jin D, Liu MM, et al. ^{19}F NMR allows the investigation of the fate of platinum(IV) prodrugs in physiological conditions. *Angew Chem Int Ed Engl* 2022;**61**:e202114250.
9. Ong JX, Le HV, Lee VEY, Ang WH. A cisplatin-selective fluorescent probe for real-time monitoring of mitochondrial platinum accumulation in living cells. *Angew Chem Int Ed Engl* 2021;**60**:9264−9.
10. Liu Y, Tian HW, Xu LY, Zhou L, Wang JH, Xu BY, et al. Investigations of the kinetics and mechanism of reduction of a carboplatin Pt(IV) prodrug by the major small-molecule reductants in human plasma. *Int J Mol Sci* 2019;**20**:20225660.
11. Wang XH, Wang XY, Jin SX, Muhammad N, Guo ZJ. Stimuli-responsive therapeutic metallodrugs. *Chem Rev* 2019;**119**:1138−92.
12. Yempala T, Babu T, Karmakar S, Nemirovski A, Ishan M, Gandin V, et al. Expanding the arsenal of Pt(IV) anticancer agents: multi-action Pt(IV) anticancer agents with bioactive ligands possessing a hydroxy functional group. *Angew Chem Int Ed Engl* 2019;**58**:18218−23.
13. Thiabaud G, He G, Sen S, Shelton KA, Baze WB, Segura L, et al. Oxaliplatin Pt(IV) prodrugs conjugated to gadolinium−texaphyrin as potential antitumor agents. *Proc Natl Acad Sci U S A* 2020;**117**:7021−9.
14. Wei DS, Huang Y, Wang B, Ma L, Karges J, Xiao HH. Photoreduction with NIR light of nucleus-targeting Pt(IV) nanoparticles for combined tumor-targeted chemotherapy and photodynamic immunotherapy. *Angew Chem Int Ed Engl* 2022;**61**:e202201486.
15. Deng ZQ, Li HC, Chen S, Wang N, Liu GY, Liu DJ, et al. Near-infrared-activated anticancer platinum(IV) complexes directly photooxidize biomolecules in an oxygen-independent manner. *Nat Chem* 2023;**15**:930−9.
16. Liang GH, Sadhukhan T, Banerjee S, Tang DS, Zhang HC, Cui MH, et al. Reduction of platinum(IV) prodrug hemoglobin nanoparticles with deeply penetrating ultrasound radiation for tumor-targeted therapeutically enhanced anticancer therapy. *Angew Chem Int Ed Engl* 2023;**62**:e202301074.
17. Jia WF, Liu R, Wang YS, Hu C, Yu WQ, Zhou Y, et al. Dual-responsive nanoparticles with transformable shape and reversible charge for amplified chemo-photodynamic therapy of breast cancer. *Acta Pharm Sin B* 2022;**12**:3354−66.
18. Dai ZW, Wang ZG. Photoactivatable platinum-based anticancer drugs: mode of photoactivation and mechanism of action. *Molecules* 2020;**25**:25215167.
19. Kwiatkowski S, Knap B, Przystupski D, Saczko J, Kedzierska E, Knap-Czop K, et al. Photodynamic therapy-mechanisms, photosensitizers and combinations. *Biomed Pharmacother* 2018;**106**:1098−107.
20. Son SB, Kim JH, Wang XW, Zhang CL, Yoon SA, Shin JW, et al. Multifunctional sonosensitizers in sonodynamic cancer therapy. *Chem Soc Rev* 2020;**49**:3244−61.
21. Zhou Y, Tong F, Gu WL, He SQ, Yang XT, Li JM, et al. Co-delivery of photosensitizer and diclofenac through sequentially responsive bilirubin nanocarriers for combating hypoxic tumors. *Acta Pharm Sin B* 2022;**12**:1416−31.
22. Han X, Zhao C, Pan ZY, Tang XY, Jiang ZQ. *N*-Doping of the TiO_2/C nanostructure derived from metal-organic frameworks with high drug loading for efficient sonodynamic & chemotherapy. *Smart Mater Med* 2022;**3**:168−78.
23. Zhu H, Yang C, Yan A, Qiang Wei, Ruan R, Ma kai, et al. Tumor-targeted nano-adjuvants to synergize photomediated immunotherapy enhanced antitumor immunity. *View* 2023;**4**:20220067.
24. Dougherty TJ, Cooper MT, Mang TS. Cutaneous phototoxic occurrences in patients receiving Photofrin. *Lasers Surg Med* 1990;**10**:485−8.
25. Lee D, Kwon S, Jang SY, Park E, Lee Y, Koo H. Overcoming the obstacles of current photodynamic therapy in tumors using nanoparticles. *Bioact Mater* 2021;**8**:20−34.
26. Mishchenko TA, Balalaeva IV, Vedunova MV, Krysko DV. Ferroptosis and photodynamic therapy synergism: enhancing anticancer treatment. *Trends Cancer* 2021;**7**:484−7.
27. Niu B, Liao KX, Zhou YX, Wen T, Quan GL, Pan X, et al. Application of glutathione depletion in cancer therapy: enhanced ROS-based therapy, ferroptosis, and chemotherapy. *Biomaterials* 2021;**277**:121110.
28. Wang HY, Qiao C, Guan QT, Wei MJ, Li ZH. Nanoparticle-mediated synergistic anticancer effect of ferroptosis and photodynamic therapy: novel insights and perspectives. *Asian J Pharm Sci* 2023;**18**:100829.
29. Wei DS, Yu YJ, Zhang XC, Wang YH, Chen H, Zhao Y, et al. Breaking the intracellular redox balance with diselenium nanoparticles for maximizing chemotherapy efficacy on patient-derived xenograft models. *ACS Nano* 2020;**14**:16984−96.
30. Sharma R, Kuche K, Thakor P, Bhavana V, Srivastava S, Mehra NK, et al. Chondroitin sulfate: emerging biomaterial for biopharmaceutical purpose and tissue engineering. *Carbohydr Polym* 2022;**286**:119305.
31. Algorri JF, Ochoa M, Roldan-Varona P, Rodriguez-Cobo L, Lopez-Higuera JM. Photodynamic therapy: a compendium of latest reviews. *Cancers (Basel)* 2021;**13**:13174447.
32. Gatti L, Cassinelli G, Zaffaroni N, Lanzi C, Perego P. New mechanisms for old drugs: insights into DNA-unrelated effects of platinum compounds and drug resistance determinants. *Drug Resist Updat* 2015;**20**:1−11.
33. Xiong YX, Xiao C, Li ZF, Yang XL. Engineering nanomedicine for glutathione depletion-augmented cancer therapy. *Chem Soc Rev* 2021;**50**:6013−41.
34. Yang WS, SriRamaratnam R, Welsch ME, Shimada K, Skouta R, Viswanathan VS, et al. Regulation of ferroptotic cancer cell death by GPX4. *Cell* 2014;**156**:317−31.
35. Tong F, Hu HL, Xu YY, Zhou Y, Xie R, Lei T, et al. Hollow copper sulfide nanoparticles carrying ISRIB for the sensitized photothermal therapy of breast cancer and brain metastases through inhibiting stress granule formation and reprogramming tumor-associated macrophages. *Acta Pharm Sin B* 2023;**13**:3471−88.